

Development of a high dynamic range spectroscopic system for observation of neutral hydrogen atom density distribution in Large Helical Device core plasma

K. Fujii, S. Atsumi, S. Watanabe, T. Shikama, M. Goto, S. Morita, and M. Hasuo

Citation: [Review of Scientific Instruments](#) **85**, 023502 (2014); doi: 10.1063/1.4863650

View online: <http://dx.doi.org/10.1063/1.4863650>

View Table of Contents: <http://scitation.aip.org/content/aip/journal/rsi/85/2?ver=pdfcov>

Published by the [AIP Publishing](#)

Articles you may be interested in

[Imaging spectroscopy diagnosis of internal electron temperature and density distributions of plasma cloud surrounding hydrogen pellet in the Large Helical Device](#)

Rev. Sci. Instrum. **83**, 093506 (2012); 10.1063/1.4751866

[Gyrokinetic turbulent transport simulation of a high ion temperature plasma in large helical device experiment](#)

Phys. Plasmas **19**, 042504 (2012); 10.1063/1.4704568

[Poloidal beam emission spectroscopy system for the measurement of density fluctuations in Large Helical Devicea\)](#)

Rev. Sci. Instrum. **81**, 10D719 (2010); 10.1063/1.3478685

[Measurement of edge density profiles of Large Helical Device plasmas using an ultrashort-pulse reflectometer](#)

Rev. Sci. Instrum. **79**, 056106 (2008); 10.1063/1.2917579

[Spatial resolved high-energy particle diagnostic system using time-of-flight neutral particle analyzer in large helical device](#)

Rev. Sci. Instrum. **74**, 1878 (2003); 10.1063/1.1537883

Nor-Cal Products



Manufacturers of High Vacuum
Components Since 1962

- Chambers
- Viewports
- Valves
- Motion Transfer
- Foreline Traps

- Flanges & Fittings
- Feedthroughs



www.n-c.com
800-824-4166

Development of a high dynamic range spectroscopic system for observation of neutral hydrogen atom density distribution in Large Helical Device core plasma

K. Fujii,^{1,a)} S. Atsumi,¹ S. Watanabe,¹ T. Shikama,¹ M. Goto,² S. Morita,² and M. Hasuo¹

¹*Department of Mechanical Engineering and Science, Graduate School of Engineering, Kyoto University, Kyoto 606-8540, Japan*

²*National Institute for Fusion Science, Toki 509-5292, Japan*

(Received 29 October 2013; accepted 14 January 2014; published online 7 February 2014)

We report development of a high dynamic range spectroscopic system comprising a spectrometer with 30% throughput and a camera with a low-noise fast-readout complementary metal-oxide semiconductor sensor. The system achieves a 10^6 dynamic range (~ 20 bit resolution) and an instrumental function approximated by a Voigt profile with Gauss and Lorentz widths of 31 and 0.31 pm, respectively, for 656 nm light. The application of the system for line profile observations of the Balmer- α emissions from high temperature plasmas generated in the Large Helical Device is also presented. In the observed line profiles, emissions are detected in far wings more than 1.0 nm away from the line center, equivalent to neutral hydrogen atom kinetic energies above 1 keV. We evaluate atom density distributions in the core plasma by analyzing the line profiles. © 2014 AIP Publishing LLC. [<http://dx.doi.org/10.1063/1.4863650>]

I. INTRODUCTION

Molecular and atomic hydrogen is ionized mainly in peripheral regions of magnetic fusion plasma, so their ionization flux is highest along plasma edges.^{1–3} Nevertheless, through charge exchange collisions with hot protons, some fraction of the atoms penetrates deep inside the plasma as neutral hydrogen and acts as a source of electrons and protons in the core region.^{4–6}

We recently investigated detailed line profiles of Balmer series emissions from high temperature plasmas generated in the Large Helical Device (LHD)⁷ and found that emissions from high temperature atoms in the core region of the plasma appear in the far wing portions of the profile, while those from the peripheral region appear in the central part.³ A method was proposed for evaluating the density distribution of neutral hydrogen atoms inside the confined region, based on the Balmer- α wing profile.⁸

Emissions from the core region are typically estimated to be $\sim 10^5$ times smaller than the peak intensity.³ Simultaneous measurement of emission intensities from peripheral and core regions requires an observation system with a dynamic range greater than 10^5 , but conventional spectroscopic systems consisting of a high-resolution spectrometer and a charge coupled device (CCD) typically provide a dynamic range of less than 10^4 , determined as the ratio of the quantum well depth of the sensor to the readout noise. Maximization of the dynamic range of observations depends on sufficient number of photons reaching the detector so that the quantum wells are nearly filled. Software averaging of multiple signals read out separately can also effectively reduce readout noise.

Here, we present our development of a high throughput spectrometer that increases the number of photons reaching

the detector without increasing exposure time. The spectrometer is equipped with high étendue camera lenses acting as collimating and focusing elements, and a transmission grism acting as a dispersion element; the throughput of the constructed spectrometer can reach 30%. When combined with a low-noise fast-readout complementary metal-oxide semiconductor (CMOS) sensor, software binning and averaging enables the system to obtain a dynamic range of up to 10^6 , with wavelength resolution of 31 pm for 656 nm light. We also describe LHD plasma observations with the system operating at 13 ms time resolution, and a method for evaluating atom density distributions in the core region based on the observed line profiles.

II. DEVELOPMENT OF THE HIGH DYNAMIC RANGE SPECTROSCOPIC SYSTEM

In the spectrometer, light output from multi-mode optical fibers is introduced through an entrance slit (schematic views, Figures 1(a-1) and 1(a-2)). The core diameter of the fibers is 400 μm and the numerical aperture for 656 nm light is about 0.20. The ends of 24 fibers are arrayed in a line along the slit, at a pitch of 500 μm . The introduced light is collimated by a camera lens (SIGMA, APO 300 mm F2.8 EX, focal length: 300 mm; F-number: 2.8) which has all glass surfaces anti-reflection coated. A long-pass filter (Hoya, R-60, cutoff wavelength: 600 nm) is mounted within the collimating lens to ensure that undesirable input to the sensor from stray light will be minimized. The collimated light beam strikes a custom-made transmission grating (Wasatch Photonics, grooves parallel to short dimension, at density N_g : 4000 grooves/mm; size: 170 \times 85 mm²) sandwiched by two identical prisms (BK7 glass, with anti-reflection coating for visible light). The dual prisms and grating combination is called a “grism” (Figures 1(b-1) and 1(b-2)). The grating is volume

^{a)}fujii@me.kyoto-u.ac.jp

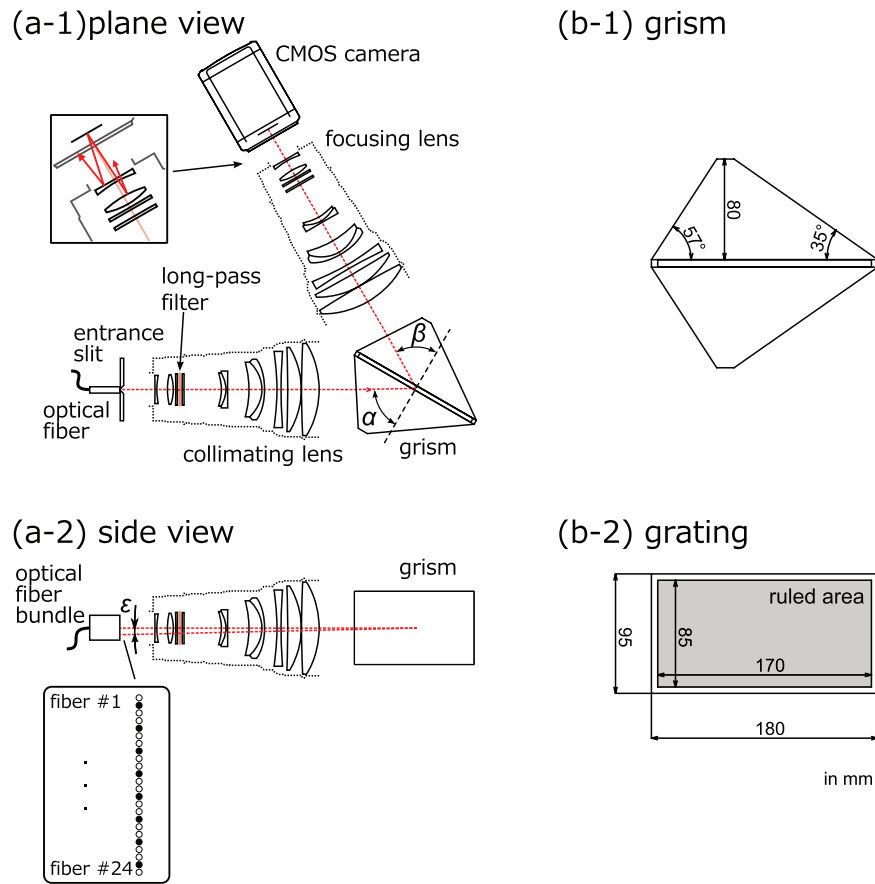


FIG. 1. Schematic illustrations of the high dynamic range spectroscopic system: (a-1) plane view and (a-2) side view. (a-1) inset: Candidate paths for stray light. (a-2) inset: Optical fiber configuration, with open circles representing optical fibers for light input and solid circles representing unused fibers. (b-1) Grism and (b-2) grism grating (dimensions in mm).

phase holographic and its diffraction efficiency is maximized for 656 nm light. The designed diffraction efficiency is 90%.

Regarding the diffraction of light by a grating, the incident angle, α , and the center angle of the diffraction, β_0 , have the following relation:⁹

$$\cos \varepsilon (\sin \alpha + \sin \beta_0) = m N_g \lambda / n, \quad (1)$$

where ε is the angle between the plane perpendicular to the rulings and the incident light beam (Figure 1(a-2)) and m is the diffraction order, with $m = 1$ in our case. λ and n are the wavelength of the particular light in a vacuum and the refractive index of the prism substrate, respectively. For 656 nm light in BK7 glass, $n = 1.51432$. We set α and β_0 to be 61.8° and 58.5° , respectively. The slight difference between α and β_0 minimizes the appearance of ghosts that are usually observed in spectrometers employing a transmission grating.¹⁰ The diffracted light beam is focused by another camera lens (SIGMA, APO 300 mm F2.8 EX).

To estimate the spectrometer throughput, we introduced Balmer- α radiation emitted from a low-pressure discharge tube (Edmund Optics, 60-906) through one of the optical fibers and compared the Balmer- α intensities measured with and without the spectrometer. The throughput with a fully opened entrance slit was estimated to be $\sim 30\%$. The finite sizes of the lens and grating mean that some light is not collimated by the lens or diffracted by the grating, and roughly

30% of the light passing through the slit is lost. The total reflection loss due to the glass surfaces of the lenses and prisms is estimated to be $\sim 20\%$. We believe that the rest of the light loss is due to the diffraction efficiency of the grism.

We use 16 optical fibers for light input, with the other fibers kept dark (Figure 1(a-2) inset). The width of the entrance slit is fixed at $30 \mu\text{m}$. The optical system brings an image of the 16 optical fiber ends into focus at the sensor surface of a CMOS camera (Hamamatsu Photonics, Orca flash-4.0, 2048×2048 pixels, pixel size: $6.75 \times 6.75 \mu\text{m}^2$). The quantum efficiency of the camera's sensor for 656 nm light is up to 70%, and the well depth corresponds to 3×10^4 photons/pixel. The camera is equipped with 16-bit AD converters and its full resolution readout rate is up to 100 frames per second. The average readout noise amplitude is estimated at 1.2 photons/pixel.

We now describe the procedure to obtain the spectrum from the focused image of the Balmer- α emission from the low-pressure discharge tube (Figure 2(a)). This image was obtained by summing 8 images and subtracting a background image that is the average of 100 images captured with no light input into any of the optical fibers. The illustrated vertical and horizontal directions are parallel to the entrance slit and direction of dispersion, respectively. The 16 bright spots aligned in a vertical line correspond to the line centers of the Balmer- α emission introduced by the 16 fibers. The centers of the spots

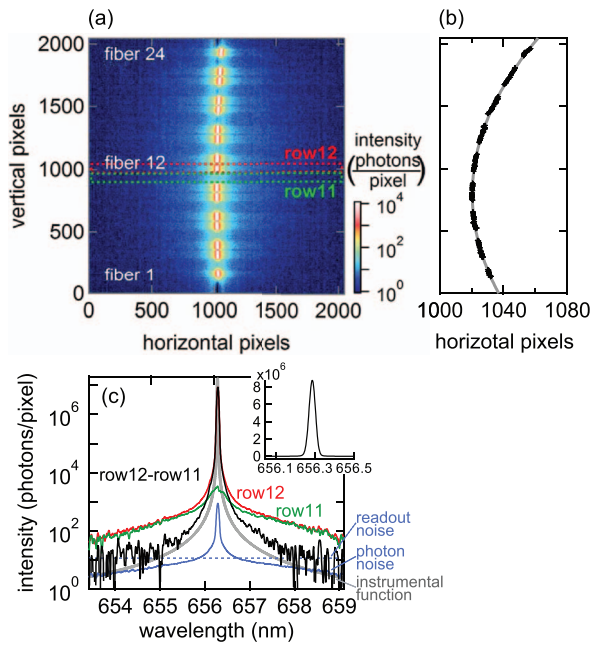


FIG. 2. (a) Two-dimensional image of the Balmer- α emission from a low-pressure hydrogen discharge tube focused on the CMOS sensor using 16 optical fiber inputs, with photons/pixel intensities shown in false colors (logarithmic intensity scale at right). The 16 vertically aligned high intensity spots correspond to the centers of the Balmer- α spectra. (b) Horizontal focus positions of 656.28 nm light on the sensor as a function of vertical pixel locations. The gray curve represents the result of a polynomial fit to the result. (c) Red curve: Spectrum obtained in the row12 region indicated in (a). The vertical scale of the intensity is logarithmic. Green curve: Profile obtained in the row11 region, considered to be stray light. Black curve: spectral profile obtained by subtraction of the signal in the row11 region from that in the row12 region. Gray curve: The instrumental function. Blue solid curve: Photon noise estimated from the spectral intensity observed in row12 and row11 regions. Blue dotted line: CMOS camera readout noise. (c) Inset: Observed spectrum using a linear scale that has a narrower wavelength range than that of main figure.

form a slight curve because of the $\cos \varepsilon$ term in Eq. (1). We fit the profile in every vertical position by means of a Gauss function that determines the center pixel of the Balmer- α emission profile (Figure 2(b)), where the bold gray curve indicates a third-order polynomial fit to the center pixels against the vertical pixel location.

In Figure 2(a), the rectangular areas enclosed by red and green dashed lines, respectively, indicated as row12 and row11, represent optical fiber #12 and #11 input regions, 66 pixels high, for the Balmer- α emission and no light, respectively. The intensities in these regions are vertically integrated by software binning that takes the image curve into account. The software binning effectively increases the quantum well depth and improves the AD conversion resolution, compared to the on-chip binning usually adopted in the CCD cameras used for spectroscopy. To further reduce statistical noise, i.e., readout noise and shot noise, we apply the moving average with a binomial weight, with a full width at half maxima (FWHM) of 11 pixels¹¹ along the horizontal direction. The results of the binning are shown in Figure 2(c) by red and green curves. Non-zero intensities are observed even in row11, and the intensity level in the wing profile of row12 is slightly higher than that of row11.

Some fraction of the light incident upon the photoelectric surface of the camera's CMOS sensor may be reflected and enter the focusing lens in a retrograde manner. Furthermore, some portion of this light is then reflected back by lens surfaces and impinges upon the CMOS sensor, as indicated in the Figure 1 (a-1) inset. Since this stray light is unfocused, the intensity distribution on the sensor is considered to have no detailed structure. We attribute intensities observed in row11 of the sensor to be due to such stray light. We assume that the intensity of stray light is the same for row11 and row12, and estimate the Balmer- α signal intensity by subtracting the intensity in row11 from that in row12, with the result shown by the black curve in Figure 2(c). The obtained spectrum has wings whose intensity is 10^6 times smaller than that of the peak.

We estimate the shot noise amplitude of the spectrum from the number of photons for each horizontal pixel by considering 8-image summations, the 66-pixel vertical summation, and the 11-pixel moving average in the horizontal direction. The readout noise amplitude is also estimated, at 10 photons/pixel. The amplitudes of the shot noise and the readout noise are, respectively, indicated by solid and dotted blue lines in Figure 2(c). The readout noise is dominant in the wing regions. Since the effective quantum well depth for each horizontal pixel included in these summations and averages is 1.6×10^7 photons/pixel, a dynamic range of over 10^6 is achieved.

We calibrated the wavelength of the system by observing the focus positions of emission lines from a thorium-argon hollow-cathode discharge tube (Heraeus, P858A), and established an absolute sensitivity calibration using a standard halogen lamp with an integration sphere (Labsphere, USS-600C).

The instrumental profile of the system is broadened by the horizontal moving average, the finite slit width, aberrations of the collimating and focusing lenses, and also by diffraction due to the finite size of optical elements in the spectrometer. We assume that the profiles of the broadenings due to the moving average, the finite slit width, and optical aberrations are Gauss functions, dominant near the profile center, while that due to diffraction is assumed to be a Lorentz function, as described in the Appendix, which is dominant in the profile wings. The resultant profile is a convolution of the Gauss and Lorentz functions, i.e., a Voigt function. We estimate the Gauss and Lorentz widths by observing several atomic emission lines, as follows.

To estimate the Gauss width of the instrumental profile, we observed the thorium emission lines of the hollow-cathode discharge tube, which has Doppler widths of less than 1 pm. The FWHM of this line is observed to be 31 pm. Without the moving average, the FWHM in this case is 14 pm.

We estimate the Lorentz width of the instrumental function based on the Fraunhofer diffraction principle.¹² When a rectangular grating of width L_g is uniformly illuminated with monochromatic light of wavelength λ_0 , the diffraction profile can be approximated by a Lorentz profile whose FWHM, w_L , is as follows:

$$w_L = \frac{\lambda_0}{\pi N_g L_g}. \quad (2)$$

In our case, w_L is calculated to be 0.31 pm; details of the approximation are described in the Appendix.

The resulting instrumental profile based on the 31 pm Gauss width and 0.31 pm Lorentz width is indicated by the gray curve in Figure 2(c). The observed Balmer- α line profile has slightly larger intensities in the wing regions than those of the instrumental function. The Lorentz width of the emission line is estimated to be 0.60 pm, using the Voigt fit of the profile and subtracting the Lorentz width of the instrumental function, a value consistent with a measurement made with a different spectrometer (THR1000, Jobin Yvon, 2400 grooves/mm; focal length: 1000 mm). The Lorentz width may be due to Stark broadening or pressure broadening of the emission line.

The Lorentz component of the instrumental function creates a certain amount of crosstalk between the peak and wing intensities in the observed emission profiles. The dynamic range of the system is limited by the Lorentz profile when the wing intensities of an emission line are small. We note that although our interest is confined to the wing intensities, knowledge of the peak intensities is necessary for evaluating the contribution of the crosstalk.

III. APPLICATION OF THE SPECTROSCOPIC SYSTEM TO LHD PLASMA OBSERVATIONS

We applied the spectroscopic system to observe hydrogen discharges in the LHD, a heliotron type of magnetic plasma confinement device at the National Institute for Fusion Science in Gifu, Japan. In the LHD, hydrogen plasma is confined by a pair of superconducting helical coils. The major radius of the magnetic axis, R_{ax} , is 3.6 m. A poloidal cross section of the LHD is shown in Figure 3, with the vacuum vessel and divertors represented as thin black curves, and magnetic flux surfaces indicated by gray ellipsoidal curves. The effective minor radius, r_{eff} , a measure of the magnetic flux surfaces,¹³ is also indicated, with $r_{eff} = 0.0$ m assigned to the magnetic axis. The effective minor radius of the last closed flux surface in the vacuum magnetic configuration is 0.60 m.

A hydrogen discharge is generated by neutral beam injection (NBI) in the LHD, and nearly stationary plasma is sustained. Electron temperature, T_e , and density, n_e , distributions are measured by the Thomson scattering method.¹⁴ The carbon ion temperature, T_i , which is considered to be similar to the proton temperature, T_p , is measured by charge exchange spectroscopy.¹⁵ The profiles shown in Figure 4(a) are repre-

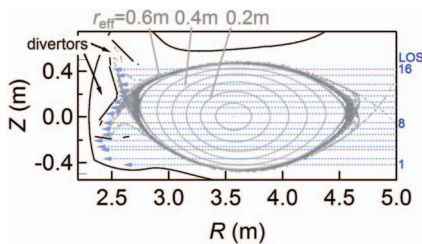


FIG. 3. Poloidal cross-section of the LHD, with gray ellipsoidal curves indicating closed magnetic flux surfaces. The locations of the ergodic layer and the divertor legs are illustrated by the gray dots outside the last closed flux surface. The horizontal arrows indicate the LOSs.

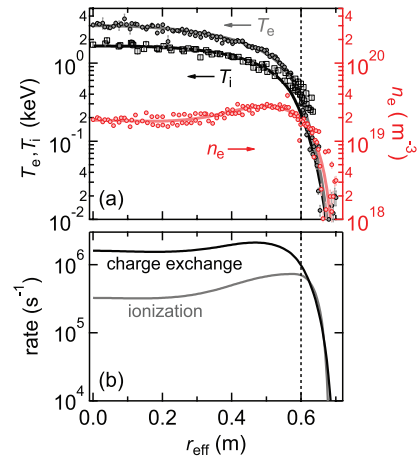


FIG. 4. (a) Circles: T_e and n_e distributions observed by the Thomson scattering method as functions of r_{eff} . Squares: T_i distribution observed by charge exchange spectroscopy. Bold curves indicate smoothed results of the distributions that are used in the spectral analysis. (b) Black and gray curves, respectively, illustrate the rates of charge exchange and ionization for hydrogen atoms, calculated from the T_e , n_e , and T_i distributions.

sented as functions of r_{eff} . The vertical dotted line in the figure shows the position of the last closed flux surface in the vacuum magnetic field. These profiles are fitted using B-splines¹⁶ and the bold curves indicate the results in Figure 4(a). We use the fitted results for the spectral analysis.

We observed the Balmer- α emission using 16 lines of sight (LOSs), represented by the 16 horizontal arrows in Figure 3 and termed LOS1, ..., LOS16, at a frame rate of 77 frames per second. The exposure time was 13 ms and the entrance slit width was 30 μ m.

Based on an assumption that the Balmer- α emission is isotropic, we estimate its line profile, $I_{polo}(\lambda)$ [photons $s^{-1} m^{-1} nm^{-1}$], from the poloidal plane toward the entire solid angle by taking the discrete integration along the Z-direction of the 16 line profiles, $I_{LOSk}(\lambda)$ [photons $s^{-1} m^{-1} sr^{-1} nm^{-1}$], $k = 1, \dots, 16$, which are observed from a single direction, and multiplying 4π as follows:

$$I_{polo}(\lambda) = \sum_{k=1}^{16} I_{LOSk}(\lambda) 4\pi \Delta Z_k, \quad (3)$$

where ΔZ_k is the interval between the lines of sight. We further assume that the spatial distribution of the Balmer- α emission is symmetric in the toroidal direction and estimate the total Balmer- α line profile from the entire LHD plasma per unit time, $I_{tot}(\lambda)$ [photons $s^{-1} nm^{-1}$], as follows:

$$I_{tot}(\lambda) = I_{polo}(\lambda) 2\pi R_{ax}. \quad (4)$$

$I_{tot}(\lambda)$ is shown in Figure 5(a) by the thin gray curve. Based on our procedure, the dynamic range of the measurement is greater than 10^6 .

In the range of 652.8–653.3 nm, the line profile is almost flat except for some impurity lines indicated by the arrows in Figure 5(a). We attribute the continuum emission to the bremsstrahlung. The estimated intensity level in this range is indicated by the horizontal gray dotted line in Figure 5(a) and this continuum emission is subtracted from the observed spectrum, with the result shown by the black solid curve in

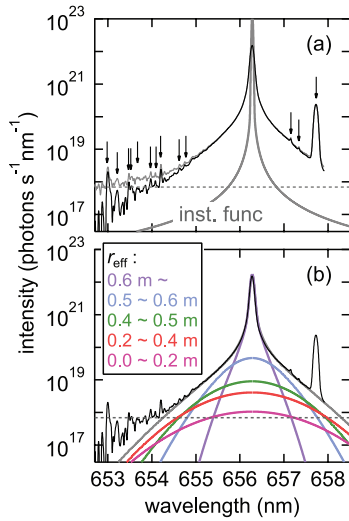


FIG. 5. (a) Gray solid curve: Observed total emission spectrum, $I_{\text{tot}}(\lambda)$. Gray dashed line: Estimated continuum level. Black curve: The Balmer- α spectrum after subtraction of continuum intensity. Vertical arrows indicate wavelengths of the line centers of the impurity lines. Bold gray curve: Instrumental function. The profile is scaled so that the area under the curve is the same as that of the observed spectrum. (b) Black curve: observed total Balmer- α spectrum after subtraction of the continuum emission. Bold gray curve: Result after fitting. Colored curves indicate estimated emission components from atom groups generated by charge exchange collisions in the r_{eff} ranges indicated in the inset.

Figure 5(a). The uncertainty of the continuum level estimate is about 20%. Even after subtraction of the continuum level, the wings in the line profiles appear to have a quasi-exponential characteristic.

In Figure 5(a), the instrumental function estimated above is also indicated by the bold gray curve, and we note that the instrumental function is scaled so that the area under the curve is the same as that of the observed spectrum. Since the observed line profile is over 100 times larger than the instrumental profile in the wing regions, the effect of the instrumental function in the wings can be ignored.

The wing profiles are a consequence of the Doppler shifted emission of high temperature neutral hydrogen atoms generated by charge exchange collisions with protons.⁷ For example, emissions appearing in wing locations 1.0 nm distant from the line center come from atoms whose velocity along the LOS is larger than 4×10^5 m/s, representing a kinetic energy of roughly 1 keV. Since charge exchange collisions are nearly pure backward collisions,¹⁷ the velocity of the generated hydrogen atoms is the same as that of the protons with which they collide. Therefore, if the proton velocity distribution is Maxwellian with temperature T_p , the generated atoms will have the same temperature. Since T_p in the core region is ~ 1.5 keV, the emissions represented in the profile wings are considered to be from such atoms generated in the core plasma.

IV. DEVELOPMENT OF A METHOD FOR EVALUATING HYDROGEN ATOM DENSITY DISTRIBUTIONS

We recently proposed a method for evaluating hydrogen atom density distributions in LHD plasmas based on observed

Balmer- α line profiles,⁸ but since the dynamic range of these observations was limited, our line profile analyses only extended from the line center to the middle of the wing portions, which reduced the accuracy of atom density measurements in the core region. In this section, we extend this method to a high dynamic range spectrum. Furthermore, in the previous method, we assumed that atoms in the core region are in equilibrium at the local proton temperature. Since the hydrogen atom density is much smaller than the proton density inside magnetically confined fusion plasmas,^{3,8} changes in the velocity of the atoms is primarily caused by charge exchange collisions with protons. The assumption of local thermal equilibrium is valid where the proton density is high enough that the mean free path of the charge exchange collisions is much smaller than the size of the plasma.

The rates of electron-impact ionization and proton-impact charge exchange collisions for the plasma observed in this work are shown in Figure 4(b). The charge exchange rate is $\sim 2 \times 10^6$ s⁻¹ in the core region. Since the typical speed of atoms generated by charge exchange collisions in the core region is $\sim 4 \times 10^5$ m/s, the mean free path was more than 0.2 m, a length comparable to the minor radius of the plasma (~ 0.6 m). This means that although the charge-exchanged atoms have almost the same velocity distribution as that of the colliding protons, the resultant local atom velocity distribution can differ from that of the protons because of the transport of the atoms and the spatial gradient of the proton temperature. The method presented here overcomes such a transport effect by considering the local “charge exchange flux,” defined below, rather than the local “atom density.” The local atom density is then determined from the charge exchange flux.

Here, we consider an atom group that is generated by charge exchange collisions in a volume with an effective minor radius of $r \sim r + \Delta r$, $\Delta V(r)$ [m³], in the LHD plasma. The number of atoms generated by collisions inside this volume per unit time, $\Delta \Phi(r)$ [s⁻¹], is proportional to the hydrogen atom density $n_H(r)$ [m⁻³] and the proton density $n_p(r)$ [m⁻³] as expressed in the following relationship:

$$\Delta \Phi(r) = r_{\text{CX}} n_p(r) n_H(r) \Delta V(r), \quad (5)$$

where r_{CX} [m³ s⁻¹] is the rate coefficient for charge exchange collisions. In this work, we ignore the small temperature dependence of the rate coefficient.¹⁷ We define $\Delta \Phi(r)$ as the charge exchange flux.

The generated hydrogen atoms travel several tens of centimeters freely through the magnetic field and then undergo ionization or charge exchange collisions. When $n_p = n_e$ is assumed, the average lifetime of atoms, τ [s], for ionization or charge exchange collisions is expressed as

$$\tau = \frac{1}{(r_{\text{CX}} + r_{\text{ion}}) \bar{n}_e}, \quad (6)$$

where r_{ion} [m³ s⁻¹] is the rate coefficient for the ionization collision. r_{ion} has been evaluated using a collisional-radiative model for hydrogen.¹⁸ The dependencies on T_e and n_e have been known to be small when $T_e > 20$ eV and $n_e < 10^{20}$ m⁻³. The average electron density along the atom’s trajectory is defined as \bar{n}_e .

Some hydrogen atoms are excited to the $n = 3$ state by electron impacts during their lifetime, where n is the principal quantum number. The probability that atoms are excited to this state, P_3 , is determined by n_e and T_e at each location and can be expressed together with a population coefficient, $R_{\text{ex}3}$ [m^3], as

$$P_3 = R_{\text{ex}3} n_e. \quad (7)$$

The excited atom density, $n_{\text{H}3}$ [m^{-3}], is described using the population coefficient as $n_{\text{H}3} = R_{\text{ex}3} n_e n_{\text{H}}$. $R_{\text{ex}3}$ has also been calculated using a collisional-radiative model as a function of n_e and T_e ,¹⁸ and its dependencies on T_e and n_e are also small when $T_e > 20$ eV and $n_e < 10^{20} \text{ m}^{-3}$. We note that in this work, we only consider the ionizing plasma, and ignore the recombination components, because ionization is dominant in the high temperature plasma where $T_e > 10$ eV.¹⁸

The probability that an atom will emit a Balmer- α photon during its lifetime, P_α [photons/atom], is expressed as

$$P_\alpha = \int_0^\tau R_{\text{ex}3} n_e A dt \cong R_{\text{ex}3} \bar{n}_e A \tau = \frac{R_{\text{ex}3} A}{r_{\text{CX}} + r_{\text{ion}}}, \quad (8)$$

where A [s^{-1}] is Einstein's A coefficient for the excited state. P_α indicates a ratio calculated as the photon emission rate coefficient divided by the sum of the charge exchange and ionization rate coefficients. This quantity is almost constant, at 0.02 photons/atom. When we assume that all the atoms are ionized in the plasma, i.e., no atoms escape from the plasma without being ionized, P_α is independent of the atom velocity and the emission location.

Since the velocity distribution of the atom group at temperature $T_p(r)$ is Maxwellian and Balmer- α photons are emitted with a constant probability of P_α , the Balmer- α emission line profile from the atom group, $\Delta I_\alpha(r, \lambda)$ [photons $\text{s}^{-1} \text{ nm}^{-1}$], is a Gauss function expressed as

$$\Delta I_\alpha(r, \lambda) = \Delta \Phi(r) P_\alpha \frac{1}{\sqrt{\pi} w(r)} \exp \left[- \left(\frac{\lambda - \lambda_0}{w(r)} \right)^2 \right], \quad (9)$$

with

$$w(r) = \lambda_0 \sqrt{\frac{2kT_p(r)}{Mc^2}}, \quad (10)$$

where M , c , and k are the atomic mass, speed of light, and Boltzmann's constant, respectively. λ_0 is the center wavelength of the Balmer- α emission line, 656.28 nm. We again note that coordinate r describes the generation locations of the atom group, not the emission locations.

The total Balmer- α emission spectrum from the entire LHD plasma, $I_{\text{tot}}(\lambda)$, is expressed as the sum of Eq. (9):

$$I_{\text{tot}}(\lambda) = \sum_{i=1}^N r_{\text{CX}} n_e(r_i) n_{\text{H}}(r_i) \Delta V(r_i) P_\alpha \frac{1}{\sqrt{\pi} w(r_i)} \times \exp \left[- \left(\frac{\lambda - \lambda_0}{w(r_i)} \right)^2 \right]. \quad (11)$$

where Eq. (5) is substituted. The above equation is a form of a discrete integration where $0 = r_1 < \dots < r_i < \dots < r_N = r_{\text{max}}$ are the discretized effective minor radii. r_{max} is the radius of

the outermost surface of the plasma where the electron density is sufficiently small. In this paper, we set $N = 30$ and $r_{\text{max}} = 0.675$ m, and we use the following equation to obtain finer spatial resolution in edge regions where steep gradients of n_e and T_e exist:

$$r_i = r_{\text{max}} \left(1 - \left(\frac{i}{N} \right)^3 \right). \quad (12)$$

Equation (11) is essentially the same as that described in Ref. 8 except that in the previous method, line integration is taken along a single line of sight, whereas volume integration is taken in this work. In Ref. 8, we deduced $n_{\text{H}}(r)$ by means of the Laplace inversion method applied to the observed line profile. Here, we deduce $n_{\text{H}}(r)$ by directly fitting the observed line profile using Eq. (11), with coefficients calculated based on the fitted results of the observed n_e and T_p distributions.

When estimating the values of a relatively large set of adjustable parameters by fitting experimental data, as we do here, small amounts of noise in the data cause the results to diverge and scatter. However, $n_{\text{H}}(r)$ must be positive and we assume that the profile of $n_{\text{H}}(r)$ is smooth. Regularization is known to be effective for suppressing such scatter, and we adopt a regularization technique usually known as the “uniform penalty” method.^{19,20} This method derives solutions that minimize the square of the sum of the spatial second derivatives of $n_{\text{H}}(r)$, as well as the χ -square between the reconstructed and observed line profile.

The bold gray curve in Figure 5(b) illustrates the line profile reconstructed using Eq. (11). We note that although we fit the short wavelength side of the profile for the reconstruction due to the carbon emission lines in the long wavelength side of the profile, the reconstructed profile appropriately represents both sides of the profile. We note further that in our present study, we cannot explain the systematic difference in the far blue wing; i.e., the 653.5–654.5 nm region in which the reconstructed profile is slightly smaller than the observed profile, although one candidate explanation is emissions of the atoms generated from non-thermal protons.²¹

Figure 6 shows the evaluated density distribution of hydrogen atoms, with the errors estimated from the uncertainty of the continuum level. The atom density in the core region is evaluated to be about 10^6 times smaller than the electron density.

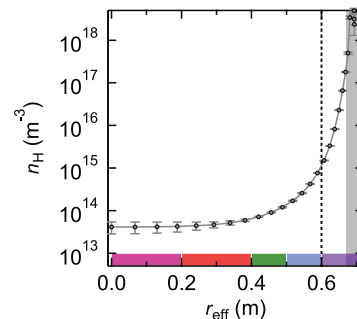


FIG. 6. Hydrogen atom density distribution estimated from the observed line profile. The gray area indicates the region where $T_p < 10$ eV and the density distribution is not deduced by the present method.

In the edge region, however, many of the atoms, generated by desorption from the walls and dissociation from molecules, emit light before they undergo charge exchange collisions. The atom temperatures generated by these desorption and dissociation processes are similar to the wall temperature, i.e., less than 0.1 eV,²² and typically 3 eV,²³ respectively. Additionally, the Zeeman effect broadens the line in the vicinity of the line center, and the temperature corresponding to this broadening is roughly 10 eV. A consequence of this effect is that our method cannot deduce the density distribution in the outmost region of the plasma, where the proton temperature is below 10 eV (the light gray region shown in Figure 6).

The spectral components due to the emission from atom groups generated by charge exchange collisions at different effective radii are shown in Figure 5(b). The emissions from the atom groups generated in the edge region are dominant near the line center, whereas emissions from those generated in core regions are dominant in the wings. We note that the $0.2 \text{ m} < r_{\text{eff}} < 0.4 \text{ m}$ component is dominant in the far wings, where intensity is 10^4 – 10^5 times smaller than the peak intensity. The emission component from $0.0 \text{ m} < r_{\text{eff}} < 0.2 \text{ m}$ is small and the uncertainty of the derived atom density there is correspondingly large, because the number of generated atoms in the center of the plasma, $\Delta\Phi(r)$, is small since $\Delta V(r)$ is nearly proportional to $r\Delta r$.

V. SUMMARY

We developed a high dynamic range spectroscopic system for accurate measurements of the Balmer- α line profile in LHD plasmas. High étendue camera lenses and a custom-made volume phase holographic grism were employed to increase the throughput of the system. A low-noise fast-readout CMOS camera was used as the light detector and a combination of software binning and the moving average provided a dynamic range of 10^6 . The instrumental function was approximated by a Voigt profile with Gauss and Lorentz widths of 31 and 0.31 pm, respectively. We applied the system to the observation of Balmer- α line profiles in high temperature plasmas generated in the LHD and presented a method for evaluating hydrogen atom density distributions based on observation of high dynamic range spectra.

ACKNOWLEDGMENTS

This work was supported by the National Institute for Fusion Science (NIFS12KOA028) and JSPS KAKENHI Grant No. 839120900004. The authors express their sincere acknowledgment to the LHD experimental group for excellent execution of the LHD experiments. One of the authors (K.F.) would like to thank the workshop in Kyoto University for manufacturing the mechanical system of the spectrometer.

APPENDIX: DIFFRACTION PROFILE PRODUCED BY A FINITE SIZE GRATING

In this appendix, we consider the diffraction profile when a light beam is truncated by a rectangular grating. A grat-

ing with length L_g and groove frequency N_g is uniformly illuminated by a monochromatic parallel light beam of wavelength λ_0/n at incident angle α . The intensity distribution of the diffracted light as a function of diffraction angle β is as follows:¹²

$$I_{\text{diff}}(\beta) \propto \text{sinc}^2 \left(\pi L_g \left(\frac{\sin \alpha + \sin \beta}{\lambda_0/n} - m N_g \right) \right), \quad (\text{A1})$$

where $\text{sinc}(x)$ is defined as $\sin(x)/x$. After substituting Eq. (1) with $\varepsilon = 0$ into the above equation, the distribution profile can be rewritten for small angle displacements $\Delta\beta$ away from the center angle of diffraction β_0 as

$$I_{\text{diff}}(\beta) \sim \text{sinc}^2(2\pi L_g(\cos \Delta\beta/(\lambda_0/n))). \quad (\text{A2})$$

Considering a light beam of wavelength $\lambda_0/n + \Delta\lambda/n$ for which the diffraction angle is $\beta_0 + \Delta\beta$, $\Delta\beta$, and $\Delta\lambda/n$ have the following relation:

$$-\cos \Delta\beta = m N_g \Delta\lambda/n. \quad (\text{A3})$$

Substituting Eq. (A2) and (A3) into (A1), the intensity distribution is now written as a function of $\Delta\lambda$:

$$I_{\text{diff}}(\Delta\lambda) \propto \text{sinc}^2(m\pi L_g N_g \Delta\lambda/\lambda_0), \quad (\text{A4})$$

where $m = 1$ in our case.

In the actual instrumental profile, other broadenings, such as those caused by the finite slit width, optical aberrations, and the horizontal moving average, are convoluted with the diffraction profile given by Eq. (A4). The widths of such broadenings are usually much larger than the spacing between the local minima of the diffraction profile. For example, in our case, the spacing between the local minima is 0.1 pm while the instrumental width is over 14 pm, even without the horizontal moving average. Furthermore, the convolution smooths out the periodic structure generated by Eq. (A4). Since, in the convolution, the function $\text{sinc}^2(x)$ approaches $1/(2x^2)$ for large values of x , and its area is π , the function can be approximated by a Lorentz function with an FWHM of 1, as follows:

$$\text{sinc}^2(x) \cong \frac{1/2}{x^2 + (1/2)^2}. \quad (\text{A5})$$

¹J. L. Weaver, B. L. Welch, H. R. Griem, J. Terry, B. Lipschultz, C. S. Pitcher, S. Wolfe, D. A. Pappas, and C. Boswell, *Rev. Sci. Instrum.* **71**, 1664 (2000).

²A. Iwamae, A. Sakaue, N. Neshi, J. Yanagibayashi, M. Hasuo, M. Goto, and S. Morita, *J. Phys. B* **43**, 144019 (2010).

³K. Fujii, T. Shikama, M. Goto, S. Morita, and M. Hasuo, *Phys. Plasmas* **20**, 012514 (2013).

⁴S. Tamor, *J. Comput. Phys.* **40**, 104 (1981).

⁵J. G. Cordey, D. G. Muir, S. V. Neudachin, V. V. Parail, E. Springmann, and A. Taroni, *Nucl. Fusion* **35**, 101 (1995).

⁶H. Takenaga, N. Asakura, K. Shimizu, S. Tsuji, M. Shimada, M. Kikuchi, K. Uchino, and K. Muraoka, *J. Nucl. Mater.* **220–222**, 429 (1995).

⁷K. Fujii, K. Mizushiri, T. Nishioka, T. Shikama, A. Iwamae, M. Goto, S. Morita, and M. Hasuo, *Nucl. Instrum. Methods Phys. Res. A* **623**, 690 (2010).

⁸M. Goto, K. Sawada, K. Fujii, M. Hasuo, and M. Morita, *Nucl. Fusion* **51**, 023005 (2011).

⁹E. Loewen, *Diffraction Grating Handbook*, 6th ed. (Newport, 2005).

¹⁰E. B. Burgh, M. A. Bershady, K. B. Westfall, and K. H. Nordsieck, *Publ. Astron. Soc. Pac.* **119**, 1069 (2007).

¹¹P. Marchand and L. Marmet, *Rev. Sci. Instrum.* **54**, 1034 (1983).

- ¹²E. Hecht, *Optics*, 4th ed. (Addison Wesley, 2001).
- ¹³C. Suzuki, K. Ida, Y. Suzuki, M. Yoshida, M. Emoto, and M. Yokoyama, *Plasma Phys. Controlled Fusion* **54**, 014016 (2012).
- ¹⁴K. Narihara, I. Yamada, H. Hayashi, and K. Yamauchi, *Rev. Sci. Instrum.* **72**, 1122 (2001).
- ¹⁵K. Ida, S. Kado, and Y. Liang, *Rev. Sci. Instrum.* **71**, 2360 (2000).
- ¹⁶C. Boor, *A Practical Guide to Splines* (Springer, New York, 2001).
- ¹⁷P. S. Krstic and D. R. Schultz, *J. Phys. B* **36**, 385 (2003).
- ¹⁸K. Sawada and T. Fujimoto, *J. Appl. Phys.* **78**, 2913 (1995).
- ¹⁹G. C. Borgia, R. J. S. Brown, and P. Fantazzini, *J. Magn. Reson.* **132**, 65 (1998).
- ²⁰P. Charbonnier, L. Blanc-Feraud, G. Aubert and M. Barlaud, *IEEE Trans. Image Process.* **6**, 298 (1997).
- ²¹Y. Luo, W. W. Heidbrink, K. H. Burrell, D. H. Kaplan, and P. Gohil, *Rev. Sci. Instrum.* **78**, 033505 (2007).
- ²²S. Brezinsek, G. Sergienko, A. Pospieszczyk, Ph. Mertens, U. Samm, and P. T. Greenland, *Plasma Phys. Controlled Fusion* **47**, 615 (2005).
- ²³M. Misakian and J. C. Zorn, *Phys. Rev. A* **6**, 2180 (1972).